THE JOURNAL OF PHYSICAL CHEMISTRY C
A JOURNAL OF THE AMERICAN CHEMICAL SOCIETY

pubs.acs.org/JPCC

Article

Ultra-High-Field ^{67}Zn and ^{33}S NMR Studies Coupled with DFT Calculations Reveal the Structure of ZnS Nanoplatelets Prepared by an Organometallic Approach

Ekaterina Bellan, Farahnaz Maleki, Martin Jakoobi, Pierre Fau, Katia Fajerwerg, Delphine Lagarde, Andrea Balocchi, Pierre Lecante, Julien Trébosc, Yijue Xu, Zhehong Gan, Lauriane Pautrot-d'Alençon, Thierry Le Mercier, Hiroki Nagashima,* Gianfranco Pacchioni, Olivier Lafon, Yannick Coppel, and Myrtil L. Kahn*

Cite This: *J. Phys. Chem. C* 2023, 127, 17809−17819

Read Online

ACCESS | Metrics & More | Article Recommendations | Supporting Information

ABSTRACT: Herein, we report the successful characterization of sulfur vacancies in ZnS nanoplatelets by in-depth high-field and DNP-enhanced solid-state NMR of ^{33}S and ^{67}Zn nuclei and DFT modeling. This two-dimensional 1 nm-thick nanomaterial was obtained by reacting a dicyclohexyl zinc complex, $ZnCy_2$, with $(TMS)_2S$ as the S source under mild conditions (45 °C) in dodecylamine. The joint experimental and theoretical studies on these nanoplatelets evidenced that a large fraction of the Zn and S atoms are located near the surface covered by dodecylamine and that the deviation from stoichiometry (agreeing with energy gap and photoluminescence properties of non-stoichiometric material) is due to sulfur vacancies. Additionally, this work reports the first ^{33}S DNP-NMR spectrum reported in the literature alongside several ultra-high-field ^{33}S and ^{67}Zn solid-state NMR spectra.

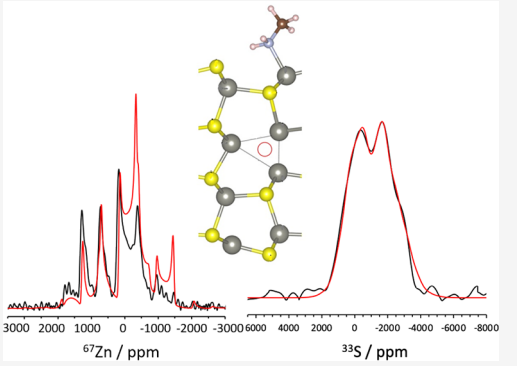

INTRODUCTION

Metal sulfide (MS) nanomaterials constitute an important class of functional materials[1,2] whose properties have great potential for applications in energy storage devices[3,4] including Li- or Zn-ion batteries,[5,6] electrochemical water splitting,[7−9] and photocatalysis.[10−12] In addition, their magnetic properties make them suitable for magneto-optic devices.[13] As such, aforementioned applications are primarily related to the MS structural variability, deriving not only from the nature of the involved transition metal but also from deviation of stoichiometry;[14] MSs have therefore attracted great attention, and numerous pathways have been designed for their synthesis.[15−18]

The basic question of interest is the interrelation between their properties and the nanoparticle (NP) size, morphology, and atomistic structure. For example, it has recently been shown that localized surface plasmon resonance (LSPR), arising from the oscillation of the electrons in the conduction band, appears not only in metallic materials but also in MS with appreciable carrier density.[19] The hole density, which is related to the stoichiometry of the MS, affects not only the LSPR intensity but also the LSPR frequency.

Of all the MSs, ZnS has been extensively studied because of its appealing electronic properties:[20−22] It exhibits a wide band gap (3.7 eV) and a high exciton binding energy (40 meV), which enable the direct conversion of electric energy into visible light, without generating heat or requiring chemical or mechanical triggers.[20−22] For these reasons, it is widely used in lasers, electroluminescent devices, flat-panel displays, field emitters, infrared windows, and UV-light detectors.[15] It is environmentally friendly and non-cytotoxic,[23] thus suggesting possible applications also in biomedicine.[24] Additionally, ZnS exhibits excellent photocatalytic capacity owing to its strong oxidation and high negative potentials of excited electrons.[25] This has been demonstrated by Peng and co-workers, who have found optimum conditions to enhance the stability and photocatalytic activity of ZnS materials,[26] while at the same time other authors have noticed an inverse effect of the amount of S vacancies on the photocatalytic activity.[27−30]

Surprisingly, the reported studies dealing with the characterization of these S vacancies at the atomic scale remain scarce and most of the results are based on theoretical calculations. This is certainly due to the difficulty in obtaining experimental evidence of these S vacancies at the atomic level.[31]

Received: April 26, 2023
Revised: August 8, 2023
Published: September 5, 2023

As a local characterization technique reaching atomic resolution, nuclear magnetic resonance (NMR) spectroscopy is a promising approach to probe the structures of vacancies. Nowadays, NMR is widely used to study the ligands at the surface of the inorganic NPs[32] or to characterize the inorganic core of NPs[33] when it contains isotopes with good receptivity, such as ^{31}P or ^{27}Al.[34] However, a major limitation of NMR spectroscopy is its lack of sensitivity, especially for isotopes with low natural abundance, low gyromagnetic ratio, and spin number $I \geq 1$, such as ^{67}Zn and ^{33}S, which often prevents the detection of most of the nuclei present in the inorganic NP cores.[35] This sensitivity issue is further exacerbated for the observation of defects, which represent a limited fraction of the NP atoms. To the best of our knowledge, no ^{33}S NMR spectrum of NPs has been reported so far, whereas ^{67}Zn NMR signals of NPs have only been detected for a few NPs, including ZnS,[36] ZnSe,[37] and ZnO.[35] Recently, we demonstrated the possibility to acquire the NMR signals of ^{67}Zn nuclei located near the surface of commercial Al-doped ZnO NPs using dynamic nuclear polarization (DNP).[38] Therefore, the NMR characterization of ZnS remains a challenge, which, if met, could provide access to new information for improving our understanding of the links between these S vacancies and the properties of the material.

Here, for the first time, the presence of S vacancies in ZnS nanoplatelets (NPls) obtained by an organometallic approach is jointly studied by DFT modeling and NMR spectroscopy.

RESULTS AND DISCUSSION

Synthesis. The preparation of colloidal ZnS NPs has been often carried out by the hot injection or heat-up methods at elevated temperatures.[39−45] Traditionally, the sources of sulfur atoms have often been elemental sulfur,[46,47] thioureas,[48−51] and thiols.[52−54] Additionally, commercially available bis-(trimethylsilyl) sulfide ($(TMS)_2S$) has been reported as a good sulfur atom precursor.[55]

Considering our previous work on the synthesis of ZnO NPs,[56−58] we reasoned that the synthesis of ZnS nanomaterials could be achieved using our $ZnCy_2$ complex as the precursor in the presence of $(TMS)_2S$ as the S source (see Figure 1).

Several experimental conditions were tested to achieve the controlled synthesis of the ZnS NPs (Table S1). Typically, $ZnCy_2$ was mixed with a given amount of the chosen ligand (*i.e.*, octylamine, OA; or dodecylamine, DDA) at a given temperature (room temperature or 45 °C), in a THF solution or in the absence of solvent. Then, $(TMS)_2S$ was introduced in the reaction vial under stirring and the reaction media was left to react from 16 up to 96 h. Under optimized reaction conditions (at 45 °C) without any added solvent, lamellar nanosheets (nanoplatelets, NPls) were reproducibly obtained. No trace of Si was detected by NMR measurement. The growth of our ultrathin NPls can be attributed to the templating effect of formed micellar structures, which has previously been reported.[59] Indeed, the TEM image shown on Figure 1 is similar to those reported by Zhang and co-workers. It is most possibly the same growth mechanism by soft templating that is responsible for this shape, the existence of a pre-organization with amines having already been suggested with organometallic precursors.[60] Compared to previously reported synthesis of ZnS lamellar nanosheets in an autoclave at 140 °C,[61] our approach allowed to obtain these nanoobjects at 45 °C and under atmospheric pressure. In addition, the

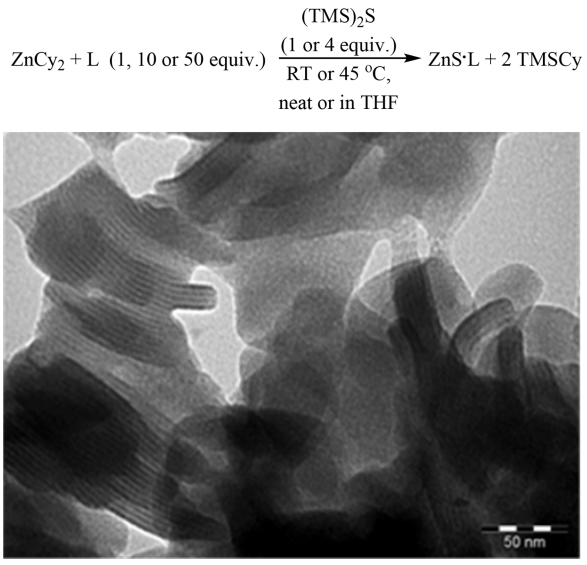

Figure 1. General reaction scheme of the synthesis of ZnS NPs (ligand (L), octylamine (OA), dodecylamine (DDA)) and TEM image of the obtained ZnS nanoplatelets under optimized conditions (*vide infra*).

contrast of the TEM images is low, possibly because of the extremely small thickness of the sheets.[62]

TEM images also show the "moiré" patterns caused by the interference between the crystalline lattices of the stacked NPls. The distance of ∼2 nm between the adjacent NPls implies the retention of capping ligands on the NPl surfaces, which was further confirmed by NMR spectroscopy (see below). Note that TEM images of ZnS particles with homogeneous contrast might also indicate small quantity of interfacial defect structures, such as stacking defects and twin structures.[63]

Structural Characterization and Physical Properties. Figure 2 shows the powder X-ray diffraction pattern of the as-

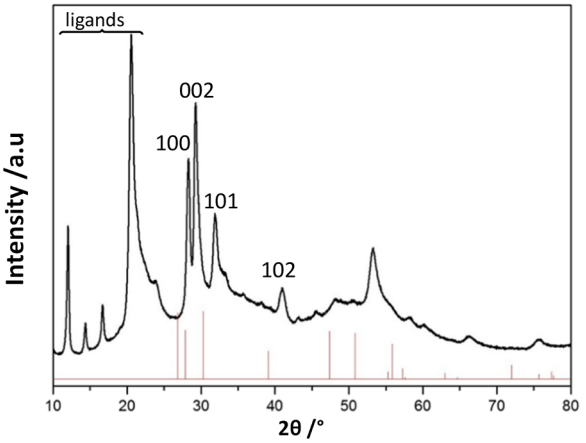

Figure 2. Powder X-ray diffraction of ZnS nanoplatelets.

obtained ZnS NPls, which corresponds to the hexagonal phase obtained usually at much higher temperatures[47] (space group P63mc). In our case, the respective peaks of ZnS NPls in the 25−80° 2θ range are shifted toward larger 2θ values, suggesting a shrinkage of the cell parameters evaluated to 3.5%. Such distortion of the network could be a consequence of the very small thickness of the NPls or eventual under

https://doi.org/10.1021/acs.jpcc.3c02754
J. Phys. Chem. C 2023, 127, 17809−17819

coordination of Zn. In addition, as already observed, additional peaks characteristic of the ligand used in the synthesis are observed at lower 2θ values (10−25°).[48]

The as-obtained ZnS NPls exhibit optical properties characteristic of small-size NPs in agreement with TEM and powder diffraction patterns. The room temperature reflectance spectrum of the powder is shown in Figure 3. Compared with

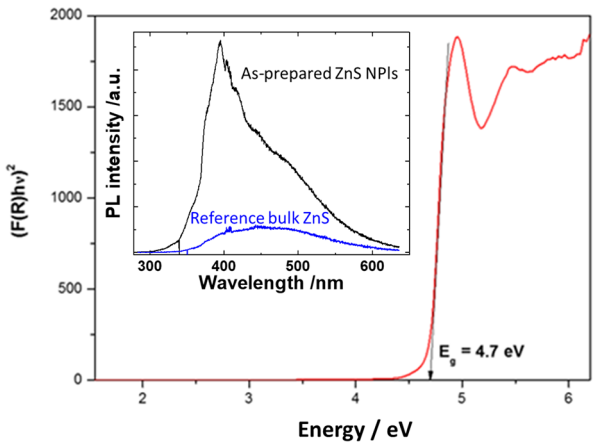

Figure 3. Optical properties of ZnS nanoplatelets: reflectance spectrum and photoluminescence spectrum (inset).

bulk ZnS for which, regardless of the polymorph, the band gap is equal to 3.68 eV, i.e., 337 nm at room temperature,[64,65] the absorption peaks for the ZnS NPls exhibits a large blue shift. An intense peak is observed at 250 nm (4.96 eV). Such a strong and narrow peak observed in the optical absorption spectrum of semiconductors is known to arise because of quantum confinement effect, which occurs in the case of NPs when the particle size becomes comparable with or smaller than the Bohr radius of exciton, i.e., bound electron−hole pairs.[66] In ZnS, assuming the effective mass of electron $m_e^* = 0.40m_e$, where m_e is the rest mass of the electron, and hole mass $m_h = 0.61m_e$ with dielectric constant $\varepsilon = 5.2$, the Bohr radius of exciton turns out to be 1.1 nm, which means that the quantum confinement effect becomes observable for NPl thickness of 1.1 nm. The photoabsorption onset corresponding to the bulk semiconductor (energy gap ∼3.54 eV) expected at about 344 nm is observed in Figure 3 at 264 nm (energy gap ∼4.7 eV), which stems also from a strong confinement effect of the exciton. This observation agrees with previously reported results.[67]

The inset of Figure 3 reports the room-temperature photoluminescence (PL) of the sample at the excitation wavelength of 275 nm. Due to the high surface-to-volume ratio in these nanostructures, the PL is characterized by a high number of peaks indicating the presence of a variety of defect-related emissions, such as surface defects, sulfur and zinc vacancies, or interstitial atoms. We observe an overall higher intensity and marked dominance of the UV-blue region for the ZnS NPl sample compared to the commercially available bulk ZnS reference. Although no consensus exists in the literature on the precise identification of the spectral lines, it has been suggested that S or Zn vacancies are at the origin of an efficient PL emission in the UV-blue region.[68,69] The higher observed intensity indicates that there are more emitting sites in the ZnS NPls than in the bulk ZnS, suggesting a larger stoichiometric deviation in the case of the NPls.

Electrical resistance measurements performed on the ZnS NPls powders, after washing processes to remove excess of ligands, show a very high electrical resistance value over 1 GΩ. Even at high temperatures—over 300 °C and up to 500 °C—the resistance of the ZnS NPls remains above several hundreds of megaohms. Generally, point defects, such as S vacancies in the structure, are associated as electron donors that can be transferred to the conduction band under thermal activation.[70,71] Similarly, Zn vacancies may act as hole carriers in the structure. However, in our case it appears that the low dimensionality of the structure limits the conductivity level due to a strong trapping of the charge carriers (either electrons or holes) associated with a very low mobility.

The optical results on the one hand, with a very high PL intensity, indicate a large number of emissive sites. On the other hand, electrical conductivity suggests the presence of defects in the material, whose nature needs to be further analyzed. Therefore, NMR spectroscopic studies in both the liquid and solid states and DFT calculations were conducted to investigate the atomic-level structure of ZnS NPls.

NMR Spectroscopic Study. The presence of DDA ligands on the ZnS NPls was probed using $^1H \rightarrow {}^{13}C$ cross-polarization under magic-angle spinning (CP-MAS) NMR experiments (Figure S1). The changes in isotropic chemical shifts (Table S2) of the CH_2 groups in the α and β positions of the amine function of the DDA ligand between DDA alone and ZnS·DDA NPls evidence the coordination of the DDA at the ZnS surface. Moreover, several ^{13}C signals of ZnS·DDA NPls, especially the CH_2 groups in the β and γ positions, are split into a major and a minor component, indicating the presence of two different types of coordinated DDA. The isotropic chemical shift of central methylene C atoms provides insights into the conformations of the alkyl chain. In the case of ZnS·DDA NPls, the isotropic chemical shift of the CH_2 group is equal to δ_{iso}^{exp}= 32.1 ppm, which indicates an all-*trans* conformation. It can be concluded that ZnS·DDA NPls has, as for DDA alone, an extended alkyl chain made of mainly methylene groups in *trans* conformation (as shown in Figure S2), in contrast to what is observed for ZnO NPs—synthesized following similar organometallic route—for which the DDA alkyl chain adopts a more bent structure with a higher population of *trans*/*gauche* or *gauche*/*gauche* conformations.[35]

To characterize the inorganic core of ZnS NPls and especially to probe the presence of defects, the NMR spectra of ^{67}Zn and ^{33}S isotopes were recorded. Figure 4 shows the ^{67}Zn signals at natural abundance of ZnS NPls by improving their detection using high magnetic fields (18.8 and 35.2 T), irradiation of the satellite transition, and quadrupolar Carr−Purcell−Meiboom−Gill (QCPMG) detection.[72,73] These spectra, for which ^{67}Zn nuclei are directly excited, contain the signals of both the surface and bulk sites. They exhibit discontinuities and cannot be simulated with a single ^{67}Zn site, which indicates the presence of different Zn local environments. Furthermore, it was not possible to simulate the two spectra acquired at two different fields using the Czjzek model,[74] which has been employed for ZnSe[37] and ZnO NPs.[35] Hence, the Zn local environments in ZnS NPls are partially ordered. Conversely, the spectra acquired at 18.8 and 35.2 T can be approximately simulated using three ^{67}Zn sites with isotropic chemical shifts, δ_{iso}^{exp}, ranging from 296 to 313 ppm and quadrupolar coupling constants, C_Q, of 2.5, 7.5, and 10 MHz, respectively (Table S3).

https://doi.org/10.1021/acs.jpcc.3c02754
J. Phys. Chem. C 2023, 127, 17809−17819

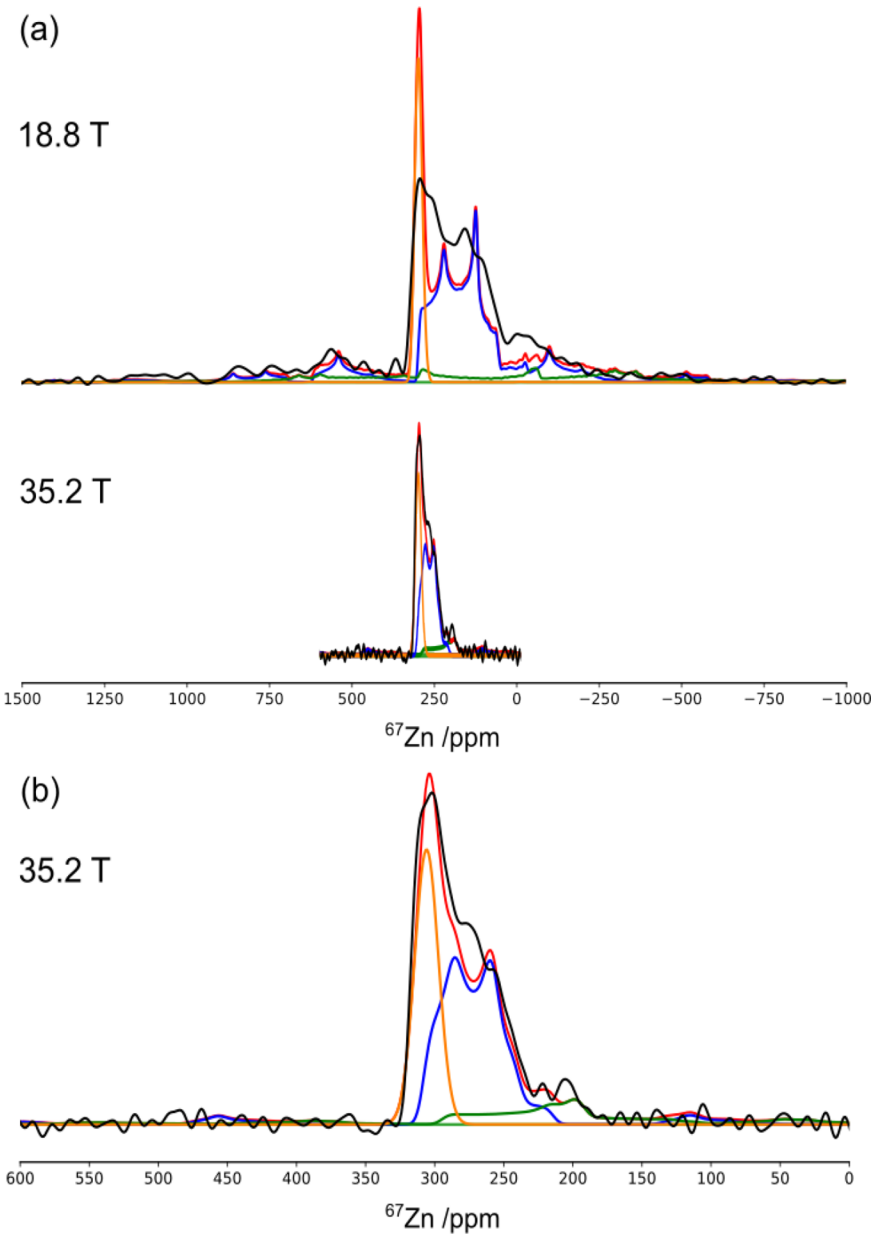

Figure 4. (a) Experimental (black) and simulated (red) conventional ^{67}Zn direct excitation spectra of pristine ZnS·DDA NPls acquired at 18.8 T (top) and 35.2 T (bottom). The simulated spectrum is the sum of three sites with C_Q = 2.5 (orange), 7.5 (blue), and 10.0 (green) MHz. (b) An expansion of the spectrum acquired at 35.2 T.

The measured isotropic chemical shifts are lower than that of ZnS_4 sites (denoted Zn_{4c} hereafter) in microcrystalline wurtzite ZnS (365 ppm).[75] Furthermore, the C_Q values are significantly higher in ZnS NPls than in microcrystalline ZnS (C_Q < 0.5 MHz), where cubic symmetry results in a vanishing quadrupolar interaction. This discrepancy indicates environment distortion breaking the cubic symmetry around ^{67}Zn nuclei,[36] such as the presence of defects or surfaces. Furthermore, the spectrum at 35.2 T exhibits a broad peak near 200 ppm. This signal is more visible in the QCPMG spikelet spectrum shown in Figure S3. This weak signal might arise from ^{67}Zn nuclei near surfaces with $C_Q \approx 10$ MHz but also near S vacancies (see DFT calculations below). No signal is detected below 180 ppm. Note that the QCPMG experiment is not quantitative since the different ^{67}Zn sites can exhibit different decays of their signal intensity during the QCPMG acquisition.

High magnetic field was also employed to acquire 1D ^{33}S direct excitation NMR spectra of ZnS NPls at 18.8 and 35.2 T (Figure 5). These spectra were simulated simultaneously as a single central transition (CT) broadened by a second-order quadrupolar interaction with best-fit parameters $\delta_{iso}^{exp} = -621$ ppm, C_Q = 5.2 MHz, and an electric field gradient (efg) asymmetry parameter, η_Q = 0.40. The presence of a single CT for ^{33}S nuclei, instead of three distinct CTs for ^{67}Zn nuclei, stems from the lower sensitivity of ^{33}S NMR parameters to the local environment, compared to those of the ^{67}Zn isotope (see DFT Computational Studies below). This lower sensitivity results from the smaller atomic number of the S element. The isotropic chemical shift is approximately 60 ppm lower than that of S_{Zn4} sites with $\delta_{iso}^{exp} = -564$ ppm in microcrystalline

https://doi.org/10.1021/acs.jpcc.3c02754
J. Phys. Chem. C 2023, 127, 17809−17819

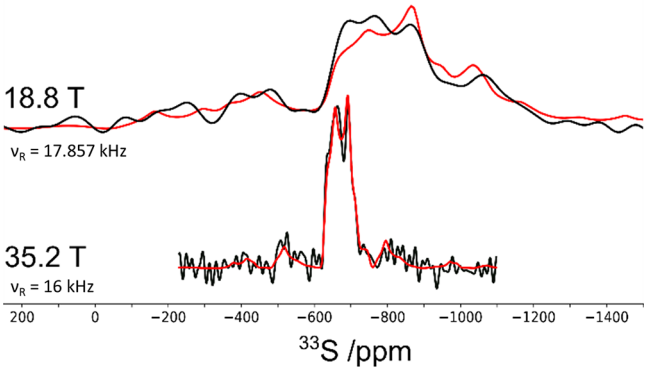

Figure 5. Experimental (black) and simulated (red) conventional ^{33}S direct excitation NMR spectra of ZnS·DDA NPls acquired at 18.8 T (top) and 35.2 T (bottom). The spectra are the FT of the sum of QCMPG echoes.

wurtzite ZnS.[76−78] Like for ^{67}Zn nuclei, the ^{33}S nuclei are subject to a much larger quadrupolar interaction in ZnS NPls than in microcrystalline wurtzite ZnS, which exhibits a vanishing quadrupolar interaction (C_Q = 0.3 MHz). The larger quadrupolar interaction in ZnS NPls stems from the presence of surface or defects, which increases the efg.

In order to observe the Zn and S sites located near the surface of ZnS·DDA NPls, we also transferred the ^{1}H magnetization to ^{67}Zn and ^{33}S nuclei using the dipolar-mediated refocused INEPT scheme (*D*-RINEPT)[38,79] and enhanced the signal using QCPMG detection along with DNP.[34,80,81] For the DNP-NMR experiments performed at 9.4 T and 105 K, the unpaired electrons were introduced in the sample by impregnating ZnS·DDA NPls with a solution of 13 mM TEKPol nitroxide biradicals in 1,1,2,2-tetrachloroethane (TCE).

The DNP-enhanced ^{1}H → ^{67}Zn *D*-RINEPT spectrum of ZnS·DDA NPls shown in Figure 6 is dominated by a manifold of narrow spinning sidebands with a centerband at 140 ppm. The centerband was identified by recording this NMR spectrum at four distinct MAS frequencies, 13.89, 12.5, 10.0, and 8.0 kHz, as shown in Figure S4. This spinning sideband manifold was simulated using a CT line shape broadened by a second-order quadrupolar interaction. As seen in Figure 6, the simulated NMR spectrum for a single site does not fully agree with the experimental one. This discrepancy might stem from different efficiencies of *D*-RINEPT transfer for the different crystallite orientations, bulk magnetic susceptibility effects due to the paramagnetic frozen radical solution,[82] and the presence of different local environments near the ZnS surface. The isotropic chemical shift is comparable to those measured in the conventional direct excitation spectrum of Figure 4, whereas the C_Q value is close to the 7.5 MHz value measured for one signal of the same spectrum. Conversely, the sites with C_Q = 2.5 MHz are not detected in the DNP-enhanced spectrum, which indicates that these sites are more distant from the ZnS surface. It should be noted that the signal with C_Q = 10 MHz is too broad at 9.4 T to be detected.

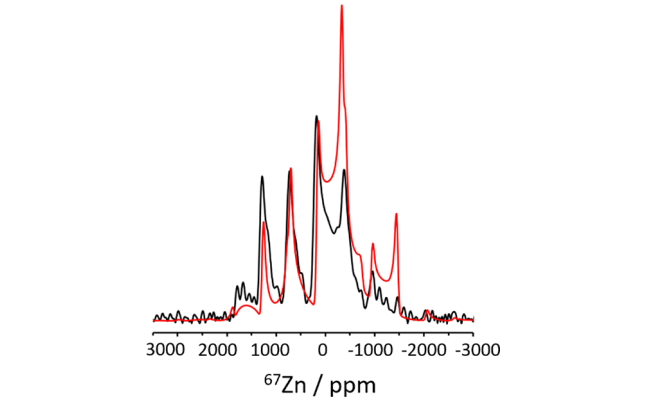

Figure 6. Experimental (black) and simulated (red) DNP-enhanced ^{1}H → ^{67}Zn *D*-RINEPT spectra of ZnS·DDA NPls impregnated with 13 mM TEKPol solution in TCE acquired at 9.4 T and 105 K with ν_R = 13.89 kHz. The spectrum was the FT of the sum of QCMPG echoes.

The sensitivity gain provided by DNP was employed to detect the NMR signals of ^{33}S nuclei located near the surface. The corresponding DNP-enhanced ^{1}H → ^{33}S *D*-RINEPT variable offset cumulative spectrum is shown in Figure 7. It

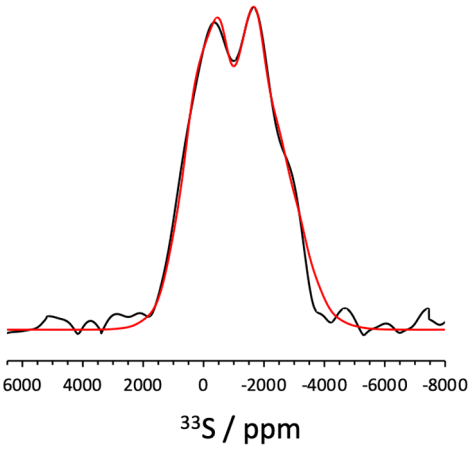

Figure 7. Experimental (black) and simulated (red) DNP-enhanced ^{1}H → ^{33}S *D*-RINEPT variable offset cumulative spectrum of ZnS·DDA NPls impregnated with 13 mM TEKPol solution in TCE acquired at 9.4 T and 105 K with ν_R = 13.89 kHz. The spectrum is the sum of four sub-spectra obtained by the FT of the sum of QCMPG echoes.

represents the first example of the ^{33}S DNP-NMR spectrum reported in the literature. This ^{33}S NMR spectrum can be simulated as a CT broadened by a second-order quadrupolar interaction with best-fit parameters δ_{iso}^{exp} = − 603 ppm, C_Q = 5.0 MHz, and η_Q = 0.55 (see Figure 7). The NMR parameters are also similar to those measured in the conventional ^{33}S direct excitation NMR spectrum of Figure 5.

DFT Computational Studies. To simulate the NMR properties of ZnS films, we used fully optimized slabs of different thicknesses: 6, 8, and 14 atomic layers, corresponding to 0.78, 1.1, and 2.1 nm thicknesses, respectively (the corresponding structures are displayed in Figure S5, Figure 8a, and Figure S6, respectively). Notice that with the notation Zn_{nS}, we refer to the number *n* of S atoms covalently bound to Zn. The results, however, are only moderately dependent on the number of layers in the slab. For each atom in the slab, we calculated using DFT the NMR parameters, δ_{iso}, C_Q, and η_Q, of ^{67}Zn and ^{33}S nuclei. A summary of the most important results extracted from the different models used in this study can be found in Table 1.

https://doi.org/10.1021/acs.jpcc.3c02754
J. Phys. Chem. C 2023, 127, 17809−17819

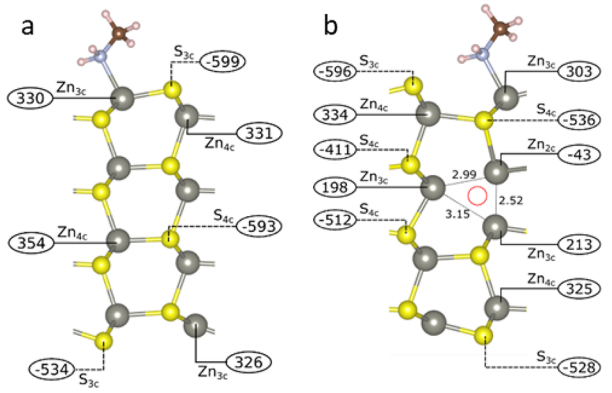

Figure 8. Side view of the 1.1 nm slab used to model ZnS NPls with a ZnS(10−10) surface and wurtzite structure with adsorbed NH_2Me molecules on one side (a) devoid of vacancy and (b) with one S vacancy created in the inner layers. The δ_{iso}^{calc} (ppm) are given for selected atoms. Zn and S atoms are displayed as gray large and yellow small spheres, respectively. For the full set of δ_{iso}^{calc}, C_Q, and η_Q values, see Tables S5 and S8.

Table 1. Overview of ^{33}S and ^{67}Zn NMR and DFT Data Obtained in This Work

NMR			
sample	nuclei	δ_{iso}^{exp} (ppm)	C_Q^{exp} (MHz)
ZnS NPls	^{67}Zn	310/313/296	2.5/7.5/10
	^{67}Zn (DNP)	320	6.7
	^{33}S	−621	5.2
	^{33}S (DNP)	−603	5.0
ZnS wurtzite bulk[74,77]	^{67}Zn	365	< 0.5
	^{33}S	−564	0.3[a]
DFT[b]			
model	atom sites	δ_{iso}^{calc} (ppm)	C_Q^{calc} (MHz)
free surface	Zn_{3c}	314 to 345	∼45.5
	S_{3c}	−538 to −528	∼7.0
free sub-surface	Zn_{4c}	325 to 342	10.5 to 11.7
	S_{4c}	−547 to −533	∼2.7
amine coordinated surface	Zn_{3c}	303 to 338	11.5 to 18.1
	S_{3c}	−602 to −571	∼6.7
amine coordinated sub-surface	Zn_{4c}	325 to 338	∼7.3
	S_{4c}	−606 to −595	∼1.6
surface site close to S-vacancies	Zn_{3c}	200 to 385	13.2 to 46.7
	Zn_{4c}	330 to 345	2.8 to 13.5
	S_{3c}	−536 to −416	4.4 to 8.2
	S_{4c}	−536 to −476	3.4 to 5.9
core site close to S-vacancies	Zn_{2c}	−43 to 35	13.8 to 34.0
	Zn_{3c}	124 to 215	1.7 to 15.2
	Zn_{4c}	320 to 390	0.9 to 4.5
	S_{4c}	−592 to −394	1.2 to 7.5
"bulk" sites	Zn_{4c}	353 to 363	0.2 to 0.6
	S_{4c}	−580 to −585	0.3 to 0.6

[a]Value calculated from ref 78. [b]The C_Q^{calc} range is based on the amplitude values ignoring the sign.

The ^{67}Zn nuclei in the most inner layers of Zn of the largest simulated slab (with a thickness of 2.1 nm, as shown in Figure S6) exhibit an isotropic chemical shift of *ca.* 360 ppm and a small C_Q value (0.17 MHz for Zn 8 in Table S6). These parameters are consistent with the experimental values obtained for microcrystalline ZnS exhibiting isotropic shifts of 365 ppm and C_Q values <0.5 MHz (Table 1). Zn_{3c} atoms of the clean surface (see Figure S6 bottom layer, Zn 14 in Table S6) have an isotropic chemical shift of 331 ppm, about 30 ppm lower than in the "bulk" but with a large C_Q value of 45 MHz. Similar isotropic chemical shifts are calculated for Zn_{4c} nuclei in the first atomic layer below the surface (Zn 2 in Table S6). The C_Q value of Zn_{4c} nuclei gradually increases from the center of the slab to the first layer below the surface (11.22 MHz for Zn 13 in Table S6).

When a very thin layer of 0.78 nm (Figure S5 and Table S4) is considered, the main features are maintained: the Zn_{3c} atoms of the clean surface have a chemical shift at 328 ppm (Zn 1 in Table S4), while Zn_{4c} in the inner layers is close to 350 ppm (Zn 3 and 4 in Table S4), consistent with their higher coordination number. A similar chemical shift of 354 ppm is computed for the Zn_{4c} atom in a 1.1 nm film (see Figure 8a and Zn 4 to 6 in Table S5). Interestingly, the average of C_Q values for ^{67}Zn nuclei in the core of slab with a thickness of 1.1 nm (Zn 3 to 6 in Table S5) is equal to 2.3 MHz, which is comparable to the smallest C_Q value (2.5 MHz) used to simulate the ^{67}Zn NMR spectra. Conversely, this average C_Q value is significantly lower (1.0 MHz) for a thickness of 2.1 nm (Zn 3 to 12 in Table S6) whereas the minimal C_Q value of 3.05 MHz for a thickness of 0.78 nm (see Table S4) exceeds that measured experimentally. Therefore, the results obtained using the 1.1 nm thin layer that are consistent with both the TEM measurements and the strong quantum confinement effect observed in the reflectance spectrum give us confidence that the DFT model is appropriate in the NMR assignments.

Interestingly, the presence of amines on the ZnS NPls does not induce a significant shift in the ^{67}Zn NMR signal whether it is NH_2Me or NH_2Et (Figure S7, Table S7) with a binding energy of 1.10 or 1.16 eV, respectively. However, amine coordination strongly reduces the C_Q value of Zn surface sites, which vary for Zn_{3c} from ca. 45 MHz (Zn 14) to ca. 12 MHz (Zn 1) and for Zn_{4c} from ca. 11 MHz (Zn 13) to ca. 7 MHz (Zn 2) (Tables S6 and S7).

The ^{67}Zn signal with $\delta_{iso}^{exp} \approx 320$ ppm, $C_Q = 6.7$ MHz, and $\eta_Q = 0.2$ detected in the DNP-enhanced NMR spectrum shown in Figure 6 stems primarily from Zn_{4c} atoms located in sub-surface layers of amine-covered ZnS NPls. These subsurface ^{67}Zn nuclei must also predominantly contribute to the signal with $C_Q = 7.5$ MHz in the direct excitation spectrum, whereas the signal with $C_Q = 10$ MHz must stem from surface sites bound to amine or sub-surface sites of the free surface. The signals of ^{67}Zn nuclei on the free surface are too broad to be detected.

To go further in the simulation of the ZnS NPls obtained by this organometallic route, we included the presence of S vacancies, which seem to be responsible for the PL emission in the UV-blue region (Figure 3). To this end, S atoms have been removed in various positions, from surface, sub-surface, and inner layers of the slab (Figure 8b and Figures S8−S11). The concentration of S vacancies was notably checked by considering supercells of different sizes, 1 × 1 and 2 × 2, containing a single vacancy, which corresponds to high (Figure S8, Table S9) and medium (Figure S9, Table S10) concentrations, respectively. The discussion refers to 14 layer slabs, but results obtained with the eight layer slabs were similar. A high concentration of S vacancies leads to the formation of Zn_{3c} and Zn_{2c} local environments, with shielded δ_{iso}^{calc} values. In particular, Zn_{3c} nuclei (bulk S vacancies) have

https://doi.org/10.1021/acs.jpcc.3c02754
J. Phys. Chem. C 2023, 127, 17809−17819

isotropic chemical shifts of approximately 170 ppm (Zn 6 and 7 in Table S9) and C_Q values between 4.8 and 10 MHz. Nevertheless, this shift can vary from 124 to 215 ppm, depending on the position of the vacancy (198−213 ppm in the 1.1 nm film, Figure 8b and Table S8). These Zn_{3c} sites could contribute to the weak signal at 200 ppm in the conventional ^{67}Zn NMR spectra (Figure 4), even if it can also stem from surface ^{67}Zn nuclei subject to large quadrupolar interaction. Two-coordinated Zn_{2c} nuclei resonate at δ_{iso}^{calc} shifts ranging from −43 to 35 ppm (17 ppm in the case shown in Figure S8). A full set of NMR data for the S vacancies at high concentrations is reported in Table S9. Interestingly, the Zn_{2c} sites do not form if the vacancies are sufficiently diluted (Figure S9, Table S10). The weak intensity around 180−200 ppm in the ^{67}Zn NMR spectrum (Figure 4) acquired at 35.2 T suggests that the ZnS NPls contain only a small amount of S vacancies since this spectrum is dominated by signals with $\delta_{iso}^{exp} \approx 310$ ppm. However, as most of the C_Q values simulated for $^{67}Zn_{3c}$ are high (between 1.7 and 15.2 MHz), these species are more difficult to observe than those subject to smaller quadrupolar interaction and, as a consequence, their amount can be underestimated. Furthermore, the small thickness of NPls does not help to evidence vacancies since ^{67}Zn nuclei near vacancies are subject to larger quadrupolar interaction near surfaces than in the core region (see Tables S8−S12). Moreover, the intensity of the $^{67}Zn_{3c}$ signal in the QCPMG spectrum may be decreased by the faster decay of their signals during the acquisition compared to other ^{67}Zn sites. Note also that some Zn_{4c} sites located close to the S vacancies (Zn 4 and 10 in Table S9; Zn 25, 26, and 31 in Table S10; Zn 8 in Table S11) have δ_{iso}^{calc} ranging between 321 and 343 ppm and C_Q values ranging between 0.6 and 4.2 MHz. For instance, the average C_Q value of the core ^{67}Zn nuclei in Table S12 is equal to 3 MHz, which is close to the 2.5 MHz value measured in the direct excitation spectrum. Finally, the central Zn_{4c} sites of ZnS NPls without defects (Figure 8a, Zn 3 to 6 in Table S5) are predicted to have δ_{iso}^{calc} above 354 ppm that does not seem compatible with the experimental NMR observations ($\delta_{iso}^{exp} \approx$ 310 ppm). These results strongly suggested that the ZnS NPls most probably include Zn close to S vacancies.

Further proof to strengthen the latter observation was obtained by the simulation of the ^{33}S NMR signals. The S_{4c} atoms of the inner layers have δ_{iso}^{calc} of −593 ppm and C_Q = 0.7 MHz (Figure 8a, S 4 in Table S5). When thicker layers were considered, the inner S_{4c} atoms had chemical shifts closer to those of the bulk microcrystalline wurtzite (−564 ppm in Table 1). For example, the S_{4c} atoms in the central layers of Figure S6 possess a δ_{iso}^{calc} = −582 ppm (S 6 and 7 in Table S6). The S_{3c} atoms of the free surface (Table 1) have δ_{iso}^{calc} values ranging from −538 to −528 ppm and C_Q = 7 MHz. The adsorption of NH_2Me molecules has a considerable effect on the isotropic chemical shift of the surface S_{3c} atoms as δ_{iso}^{calc} becomes −599 ppm (Figure 8a, S 1 in Table S5), whereas the C_Q value is only slightly affected. Remarkably, the isotropic chemical shift values calculated around −600 ppm are more shielded than the values measured for microcrystalline wurtzite. On the other hand, the C_Q value of about 7 MHz calculated for the surface sites is consistent with the experimental parameters to simulate the conventional ^{33}S NMR signal (δ_{iso}^{exp} = −621 ppm, C_Q = 5.2 MHz) in Figure 5 and the DNP-enhanced NMR ^{33}S NMR signal in Figure 7 (δ_{iso}^{exp} = −603 ppm and C_Q = 5.0 MHz). This strongly suggests that a large fraction of the S atoms are located close to the surfaces where amine ligands are present.

Calculations of ^{33}S NMR parameters for ZnS NPls containing S vacancies were also performed (see Figures S8−S11). For high concentrations of vacancy or vacancy aggregations, we found S_{4c} nuclei near S vacancies with δ_{iso}^{calc} of −421 and −465 ppm (C_Q = −7.5 and −5.4 MHz, respectively), as seen in Figure S8 and Table S9. For diluted S vacancies (see Figure S9), the S_{4c} nuclei near S vacancies exhibit chemical shifts around −534 and −561 ppm and C_Q values ranging from −5 to −7 MHz. For a 1.1 nm-thick ZnS slab with adsorbed NH_2Me molecules (see Figure 8b and Table S8), δ_{iso}^{calc} is of −411 and −512 ppm (C_Q = −4.8 and −3.8 MHz, respectively). We can also note that for ZnS NPls without defects (S 3 to 6 in Table S5), core S_{4c} nuclei are predicted to have δ_{iso}^{calc} between −573 and −593 ppm with small C_Q values (less than 1.1 MHz) that do not seem to be compatible with the NMR observations, especially for the C_Q values. Indeed, the presence of defects increases the C_Q values (between 2.6 and 5.4 MHz) of S_{4c} nuclei close to the vacancies (S 9 in Table S9; S 23 to 28, 34, and 36 in Table S10; S 9 in Table S11). Unfortunately, the resolution and sensitivity of the ^{33}S spectra at natural abundance even at 35.2 T are not good enough to be able to clearly evidence the S_{4c} nuclei close to S vacancies with deshielded resonances (from −561 up to −386 ppm) and high C_Q absolute values of >4 MHz. However, the absence of a ^{33}S signal with weak C_Q is consistent with the presence of vacancies inside the core of ZnS NPls.

To summarize, the proposed model consists of a 1 nm-thickness ZnS film with coordinated amine ligands, and a low but significant concentration of S vacancies. The majority of Zn sites have chemical shifts (296 ppm $\leq \delta_{iso}^{exp} \leq$ 313 ppm) and C_Q values (2.5 MHz $\leq C_Q$) significantly different from bulk Zn_{4c} sites (δ_{iso}^{exp} = 365 ppm and C_Q < 0.5 MHz) but in agreement with Zn_{4c} sites close to the amine-bound surface of ZnS and to S vacancies. The C_Q value was even higher (6.7 MHz) for the Zn sites closest to the surface evidenced by the DNP-enhanced ^{1}H → ^{67}Zn *D*-RINEPT experiment. The presence of S vacancies also lowered the δ_{iso}^{calc} of Zn_{4c} sites close to them (mostly between 320 and 345 ppm) and increased the C_Q values (between 0.9 and 13.5 MHz) compared to bulk Zn_{4c} sites. Zn_{3c} nuclei in contact to S vacancies were also potentially observed under a weak ^{67}Zn NMR signal around 180−200 ppm. Due to a lack of resolution and sensitivity even at 35.2 T, the ^{33}S NMR spectra are less informative. Most of the S sites detected by ^{33}S NMR have a chemical shift and C_Q (δ_{iso}^{exp} = −621 ppm, C_Q = 5.2 MHz) in agreement with S_{3c} and S_{4c} atoms at or close to the amine-bound surface of ZnS (δ_{iso}^{calc} around −600 ppm, C_Q up to 6.7 MHz) and significantly different from bulk S_{4c} sites (δ_{iso}^{exp} = −564 ppm and $C_Q \sim$ 0.3 MHz). The presence of S vacancies leads also to an increase of C_Q values (up to 8.7 MHz) for S_{4c} sites close to them but should additionally lead to an increase of δ_{iso}^{calc} (up to −386 ppm). Overall, our model of ZnS NPls of about 1 nm with coordinated amine ligands and S vacancies reproduces the majority of the NMR data and is consistent with the results of the optical and conductive properties. In particular, the presence of S vacancies is supported by experimental ^{33}S C_Q constant values and ^{67}Zn isotropic chemical shifts, higher and lower, respectively, than those calculated for ZnS nanoplatelets devoid of S vacancies (see Table S5) but also by the observation of the ^{67}Zn signal near 200 ppm and efficient PL emission in the UV-blue region (Figure 3).

https://doi.org/10.1021/acs.jpcc.3c02754
J. Phys. Chem. C 2023, 127, 17809−17819

CONCLUSIONS

In this work, ^{67}Zn and ^{33}S solid-state NMR experiments at ultra-high fields and DNP experimental data coupled with DFT calculations allowed for the first time to propose a structural model in full agreement with the observed optical and conductive properties of ZnS nanoplatelets. This nanomaterial obtained by an organometallic approach under mild conditions consists of ZnS nanoplatelets with a thickness of 1 nm covered by DDA. These nanoplatelets contained defects based on sulfur vacancies, and their presence was evidenced in PL and electrical resistance measurements. Furthermore, this study represents a step toward the use of NMR spectroscopy coupled with DFT calculations for a better understanding of the structure−property relationship of MS nanocrystals, a very large family of materials with broad potential uses.

ASSOCIATED CONTENT

Supporting Information

The Supporting Information is available free of charge at https://pubs.acs.org/doi/10.1021/acs.jpcc.3c02754.

Experimental section; experimental conditions for ZnS preparation; $^{1}H \rightarrow {}^{13}C$ CP-MAS spectra of ZnS·DDA NPls and pristine DDA; ^{13}C isotropic chemical shifts in ppm of ZnS·DDA NPls and pristine DDA; proposed models for the conformation of DDA on the ZnS NPl surface; parameters of the fitting of Figure 4; experimental conventional ^{67}Zn direct excitation spectra of pristine ZnS·DDA NPls acquired at 35.2 T and ν_R = 16 kHz; experimental DNP-enhanced $^{1}H \rightarrow {}^{67}Zn$ D-RINEPT spectrum of ZnS·DDA NPls at different MAS frequencies; side views of the slabs used to model ZnS NPls with 6 or 14 layers, different concentrations of S vacancies and NH_2Me or NH_2Et ligands (PDF)

AUTHOR INFORMATION

Corresponding Authors

Hiroki Nagashima − *Interdisciplinary Research Center for Catalytic Chemistry, National Institute of Advanced Industrial Science and Technology (AIST), Tsukuba, Ibaraki 305-8565, Japan;* orcid.org/0000-0002-7042-9051; Email: nagashima-hiroki@aist.go.jp

Myrtil L. Kahn − *LCC-CNRS, Université de Toulouse, CNRS, UPS, Toulouse 31077, France;* orcid.org/0000-0003-3079-5759; Email: myrtil.kahn@lcc-toulouse.fr

Authors

Ekaterina Bellan − *LCC-CNRS, Université de Toulouse, CNRS, UPS, Toulouse 31077, France*

Farahnaz Maleki − *Dipartimento di Scienza dei Materiali, Università di Milano − Bicocca, Milano 20125, Italy;* orcid.org/0000-0002-5747-1319

Martin Jakoobi − *LCC-CNRS, Université de Toulouse, CNRS, UPS, Toulouse 31077, France;* orcid.org/0000-0002-6181-4839

Pierre Fau − *LCC-CNRS, Université de Toulouse, CNRS, UPS, Toulouse 31077, France;* orcid.org/0000-0003-0014-2511

Katia Fajerwerg − *LCC-CNRS, Université de Toulouse, CNRS, UPS, Toulouse 31077, France;* orcid.org/0000-0002-3897-3380

Delphine Lagarde − *LPCNO, INSA, UPS, Toulouse 31077, France*

Andrea Balocchi − *LPCNO, INSA, UPS, Toulouse 31077, France*

Pierre Lecante − *CEMES, UPS, Toulouse 31055, France*

Julien Trébosc − *Université de Lille, CNRS, INRAE, Centrale Lille, Université d'Artois, FR 2638 − IMEC − Fédération Chevreul, Lille 59000, France*

Yijue Xu − *National High Magnetic Field Laboratory, Tallahassee, Florida 32310, United States*

Zhehong Gan − *National High Magnetic Field Laboratory, Tallahassee, Florida 32310, United States;* orcid.org/0000-0002-9855-5113

Lauriane Pautrot-d'Alençon − *Solvay, Research and Innovation Centre de Paris, Aubervilliers 93308, France*

Thierry Le Mercier − *Solvay, Research and Innovation Centre de Paris, Aubervilliers 93308, France*

Gianfranco Pacchioni − *Dipartimento di Scienza dei Materiali, Università di Milano − Bicocca, Milano 20125, Italy;* orcid.org/0000-0002-4749-0751

Olivier Lafon − *Université de Lille, CNRS, Centrale Lille, Université d'Artois, UMR 8181 − UCCS − Unité de Catalyse et Chimie du Solide, Lille 59000, France;* orcid.org/0000-0002-5214-4060

Yannick Coppel − *LCC-CNRS, Université de Toulouse, CNRS, UPS, Toulouse 31077, France;* orcid.org/0000-0003-0970-4082

Complete contact information is available at: https://pubs.acs.org/10.1021/acs.jpcc.3c02754

Author Contributions

L.P., T.L.M., and M.L.K conceived this program. E.B. and M.J. synthesized the material. K.F. participated to the characterization. P.F. carried out the conductivity measurements. P.L. analyzed the XRD measurements. H.N., Y.X., Z.G., J.T., O.L., and Y.C. performed and analyzed the NMR experiments. F.M. and G.P. performed the DFT simulations. M.L.K, O.L., Y.C., and G.P. wrote the article. All authors valuably contributed to the discussions and approved the final version of the manuscript.

Notes

The authors declare no competing financial interest.

ACKNOWLEDGMENTS

The work was supported by the CNRS, the Université de Toulouse. Solvay, Chevreul Institute (FR 2638), Ministère de l'Enseignement Supérieur, de la Recherche et de l'Innovation, Hauts-de-France Region, and FEDER are acknowledged for supporting and funding partially this work. Financial support from the IR INFRANALYTICS FR2054 for conducting the research is gratefully acknowledged. The National High Magnetic Field Laboratory is supported by the National Science Foundation through NSF/DMR-1644779 and the State of Florida. The Development of the 36 T Series-Connected Hybrid magnet and NMR instrumentation was supported by NSF (DMR-1039938 and DMR-0603042) and NIH GM122698. F.M. and G.P. thank the financial support from the Italian Ministry of University and Research (MIUR) through the PRIN Project 20179337R7. H.N. acknowledges JSPS Grant-in-Aid for Early-Career Scientists (JP20K15319) and JST, PRESTO Grant Number JPMJPR2276, Japan, for DNP-NMR experiments. Thanks are due to Vincent Collière for TEM images and Christine Lepetit for providing Figure S2.

■ ABBREVIATIONS

MS; metal sulfide; NP; nanoparticles; LSPR; localized surface plasmon resonance; NMR; nuclear magnetic resonance; NPls; nanoplatelets; OA; octylamine; DDA; dodecylamine; efg; electric field gradient; TCE; 1,1,2,2-tetrachloroethane

■ REFERENCES

(1) Glotov, A.; Vutolkina, A.; Pimerzin, A.; Vinokurov, V.; Lvov, Y. Clay nanotube-metal core/shell catalysts for hydroprocesses. *Chem. Soc. Rev.* **2021**, *50*, 9240.

(2) Wang, J.; Lin, S.; Tian, N.; Ma, T.; Zhang, Y.; Huang, H. Nanostructured Metal Sulfides: Classification, Modification Strategy, and Solar-Driven CO_2 Reduction Application. *Adv. Funct. Mater.* **2021**, *31*, 2008008.

(3) Xue, G.; Bai, T.; Wang, W.; Wang, S.; Ye, M. Recent advances in various applications of nickel cobalt sulfide-based materials. *J. Mater. Chem. A* **2022**, *10*, 8087.

(4) Thangavel, R.; Ganesan, B. K.; Thangavel, V.; Yoon, W.-S.; Lee, Y.-S. Emerging Materials for Sodium-Ion Hybrid Capacitors: A Brief Review. *ACS Appl. Energy Mater.* **2021**, *4*, 13376.

(5) Hwang, J.; Matsumoto, K.; Chen, C.-Y.; Hagiwara, R. Pseudo-solid-state electrolytes utilizing the ionic liquid family for rechargeable batteries. *Energy Environ. Sci.* **2021**, *14*, 5834.

(6) Wu, J.; Ye, T.; Wang, Y.; Yang, P.; Wang, Q.; Kuang, W.; Chen, X.; Duan, G.; Yu, L.; Jin, Z.; et al. Understanding the Catalytic Kinetics of Polysulfide Redox Reactions on Transition Metal Compounds in Li−S Batteries. *ACS Nano* **2022**, *16*, 15734.

(7) Zhang, H.; Zhou, Y.; Xu, M.; Chen, A.; Ni, Z.; Akdim, O.; Wågberg, T.; Huang, X.; Hu, G. Interface Engineering on Amorphous/Crystalline Hydroxides/Sulfides Heterostructure Nanoarrays for Enhanced Solar Water Splitting. *ACS Nano* **2023**, *17*, 636.

(8) Li, H.; Han, X.; Zhao, W.; Azhar, A.; Jeong, S.; Jeong, D.; Na, J.; Wang, S.; Yu, J.; Yamauchi, Y. Electrochemical preparation of nano/micron structure transition metal-based catalysts for the oxygen evolution reaction. *Mater. Horiz.* **2022**, *9*, 1788.

(9) da Silva, M. I.; Machado, I. R.; Toma, H. E.; Araki, K.; Angnes, L.; Gonçalves, J. M. Recent progress in water-splitting and supercapacitor electrode materials based on MOF-derived sulfides. *J. Mater. Chem. A* **2022**, *10*, 430.

(10) Li, Y.; Lai, C.; Liu, S.; Fu, Y.; Qin, L.; Xu, M.; Ma, D.; Zhou, X.; Xu, F.; Liu, H.; et al. Metallic active-site engineering: a bridge between covalent triazine frameworks and high-performance catalysts. *J. Mater. Chem. A* **2023**, *11*, 2070.

(11) Vakalopoulou, E.; Rath, T.; Kräuter, M.; Torvisco, A.; Fischer, R. C.; Kunert, B.; Resel, R.; Schröttner, H.; Coclite, A. M.; Amenitsch, H.; et al. Metal Sulfide Thin Films with Tunable Nanoporosity for Photocatalytic Applications. *ACS Appl. Nano Mater.* **2022**, *5*, 1508.

(12) Cabana, J.; Monconduit, L.; Larcher, D.; Palacin, M. R. Beyond Intercalation-Based Li-Ion Batteries: The State of the Art and Challenges of Electrode Materials Reacting Through Conversion Reactions. *Adv. Mater.* **2010**, *22*, No. E170.

(13) Boncher, W.; Dalafu, H.; Rosa, N.; Stoll, S. Europium chalcogenide magnetic semiconductor nanostructures. *Coord. Chem. Rev.* **2015**, *289*, 279.

(14) Gross, S.; Vittadini, A.; Dengo, N. Functionalisation of Colloidal Transition Metal Sulphides Nanocrystals: A Fascinating and Challenging Playground for the Chemist. *Crystals* **2017**, *7*, 110.

(15) Fang, X.; Wu, L.; Hu, L. ZnS Nanostructure Arrays: A Developing Material Star. *Adv. Mater.* **2011**, *23*, 585.

(16) Yin, L.-W.; Bando, Y.; Zhan, J.-H.; Li, M.-S.; Golberg, D. Self-Assembled Highly Faceted Wurtzite-Type ZnS Single-Crystalline Nanotubes with Hexagonal Cross-Sections. *Adv. Mater.* **2005**, *17*, 1972.

(17) Sarker, J. C.; Hogarth, G. Dithiocarbamate Complexes as Single Source Precursors to Nanoscale Binary, Ternary and Quaternary Metal Sulfides. *Chem. Rev.* **2021**, *121*, 6057.

(18) Liu, X.; Li, Y.; Cao, Z.; Yin, Z.; Ma, T.; Chen, S. Current progress of metal sulfides derived from metal−organic frameworks for advanced electrocatalysis: potential electrocatalysts with diverse applications. *J. Mater. Chem. A* **2022**, *10*, 1617.

(19) Luther, J. M.; Jain, P. K.; Ewers, T.; Alivisatos, A. P. Localized surface plasmon resonances arising from free carriers in doped quantum dots. *Nat. Mater.* **2011**, *10*, 361.

(20) Lange, T.; Reichenberger, S.; Ristig, S.; Rohe, M.; Strunk, J.; Barcikowski, S.; Schlögl, R. Zinc sulfide for photocatalysis: White angel or black sheep? *Prog. Mater. Sci.* **2022**, *124*, No. 100865.

(21) Hu, Z.; O'Neill, R.; Lesyuk, R.; Klinke, C. Colloidal Two-Dimensional Metal Chalcogenides: Realization and Application of the Structural Anisotropy *Acc. Chem. Res.* **2021**, *54*, 3792.

(22) Fang, X.; Zhai, T.; Gautam, U. K.; Li, L.; Wu, L.; Bando, Y.; Golberg, D. ZnS nanostructures: From synthesis to applications. *Prog. Mater. Sci.* **2011**, *56*, 175.

(23) Sluydts, M.; De Nolf, K.; Van Speybroeck, V.; Cottenier, S.; Hens, Z. Ligand Addition Energies and the Stoichiometry of Colloidal Nanocrystals. *ACS Nano* **2016**, *10*, 1462.

(24) Hu, J.; Bando, Y.; Zhan, J.; Golberg, D. Sn-Filled Single-Crystalline Wurtzite-Type ZnS Nanotubes. *Angew. Chem., Int. Ed.* **2004**, *43*, 4606.

(25) Rameshbabu, R.; Ravi, P.; Sathish, M. Cauliflower-like CuS/ZnS nanocomposites decorated g-C_3N_4 nanosheets as noble metal-free photocatalyst for superior photocatalytic water splitting. *Chem. Eng. J.* **2018**, *176*, 678.

(26) Peng, H.; Liu, D.; Zheng, X.; Fu, X. *Nanomaterials* **2019**, *9*, 1657.

(27) Joo, J.; Na, H. B.; Yu, T.; Yu, J. H.; Kim, Y. W.; Wu, F.; Zhang, J. Z.; Hyeon, T. Generalized and Facile Synthesis of Semiconducting Metal Sulfide Nanocrystals. *J. Am. Chem. Soc.* **2003**, *125*, 11100.

(28) Zhang, C.; Zhou, Y.; Bao, J.; Fang, J.; Zhao, S.; Zhang, Y.; Sheng, X.; Chen, W. Structure regulation of ZnS@g-C_3N_4/TiO_2 nanospheres for efficient photocatalytic H_2 production under visible-light irradiation. *Chem. Eng. J.* **2018**, *346*, 226.

(29) Hu, X.; Deng, F.; Huang, W.; Zeng, G.; Luo, X.; Dionysiou, D. D. The band structure control of visible-light-driven rGO/ZnS-MoS_2 for excellent photocatalytic degradation performance and long-term stability. *Chem. Eng. J.* **2018**, *350*, 248.

(30) Li, P.; He, T. Common-cation based Z-scheme ZnS@ZnO core-shell nanostructure for e_cient solar-fuel production. *Appl. Catal., B* **2018**, *238*, 518.

(31) Mourdikoudis, S.; Pallares, R. M.; Thanh, N. T. K. Characterization techniques for nanoparticles: comparison and complementarity upon studying nanoparticle properties. *Nanoscale* **2018**, *10*, 12871.

(32) Coppel, Y.; Spataro, G.; Pagés, C.; Chaudret, B.; Maisonnat, A.; Kahn, M. L. Full Characterization of Colloidal Solutions of Long-Alkyl-Chain-Amine-Stabilized ZnO Nanoparticles by NMR Spectroscopy: Surface State, Equilibria, and Affinity. *Chem. − Eur. J.* **2012**, *18*, 5384.

(33) Champouret, Y.; Coppel, Y.; Kahn, M. L. Evidence for Core Oxygen Dynamics and Exchange in Metal Oxide Nanocrystals from In Situ ^{17}O MAS NMR. *J. Am. Chem. Soc.* **2016**, *138*, 16322.

(34) Rankin, A. G. M.; Trébosc, J.; Pourpoint, F.; Amoureux, J.-P.; Lafon, O. Recent developments in MAS DNP-NMR of materials. *Solid State Nucl. Magn. Reson.* **2019**, *101*, 116.

(35) Spataro, G.; Champouret, Y.; Florian, P.; Coppel, Y.; Kahn, M. L. Multinuclear solid state NMR spectroscopy: a powerful tool for understanding of structure and dynamics of ZnO hybrid nanomaterials. *Phys. Chem. Chem. Phys.* **2018**, *20*, 12413.

(36) Tang, H.-Y.; Lin, C.-C.; Wang, L.-S.; Yang, W.-C.; Liao, K.-H.; Li, F.-Y.; Liao, M.-Y. Quantum size effect on ^{67}Zn-NMR measurements of ZnS nanoparticles. *Phys. Rev. B* **2008**, *77*, No. 165420.

(37) Cadars, S.; Smith, B. J.; Epping, J. D.; Acharya, S.; Belman, N.; Golan, Y.; Chmelka, B. F. Atomic positional versus electronic order in semiconducting ZnSe nanoparticles. *Phys. Rev. Lett.* **2009**, *103*, No. 136802.

(38) Nagashima, H.; Trebosc, J.; Kon, Y.; Sato, K.; Lafon, O.; Amoureux, J.-P. Observation of Low-γ Quadrupolar Nuclei by

https://doi.org/10.1021/acs.jpcc.3c02754
J. Phys. Chem. C 2023, 127, 17809−17819

Surface-Enhanced NMR Spectroscopy. *J. Am. Chem. Soc.* **2020**, *142*, 10659.
(39) Panda, A. B.; Acharya, S.; Efrima, S.; Golan, Y. Synthesis, assembly, and optical properties of shape- and phase-controlled ZnSe nanostructures. *Langmuir* **2007**, *23*, 765.
(40) Pradhan, N.; Peng, X. Efficient and Color-Tunable Mn-Doped ZnSe Nanocrystal Emitters: Control of Optical Performance via Greener Synthetic Chemistry. *J. Am. Chem. Soc.* **2007**, *129*, 3339.
(41) Acharya, S.; Sarma, D. D.; Jana, N. R.; Pradhan, N. An Alternate Route to High-Quality ZnSe and Mn-Doped ZnSe Nanocrystals. *J. Phys. Chem. Lett.* **2010**, *1*, 485.
(42) Jia, G.; Banin, U. A General Strategy for Synthesizing Colloidal Semiconductor Zinc Chalcogenide Quantum Rods. *J. Am. Chem. Soc.* **2014**, *136*, 11121.
(43) Acharya, S.; Sarkar, S.; Pradhan, N. Material Diffusion and Doping of Mn in Wurtzite ZnSe Nanorods. *J. Phys. Chem. C* **2013**, *117*, 6006.
(44) Flamee, S.; Cirillo, M.; Abe, S.; Nolf, K. D.; Gomes, R.; Aubert, T.; Hens, Z. Fast, High Yield, and High Solid Loading Synthesis of Metal Selenide Nanocrystals. *Chem. Mater.* **2013**, *25*, 2476−2483.
(45) Quan, Z.; Wang, Z.; Yang, P.; Lin, J.; Fang, J. Synthesis and Characterization of High-Quality ZnS, ZnS:Mn^{2+}, and ZnS:Mn^{2+}/ZnS (Core/Shell) Luminescent Nanocrystals. *Inorg. Chem.* **2007**, *46*, 1354.
(46) Deng, Z.; Tong, L.; Flores, M.; Lin, S.; Cheng, J.-X.; Yan, H.; Liu, Y. High-Quality Manganese-Doped Zinc Sulfide Quantum Rods with Tunable Dual-Color and Multiphoton Emissions. *J. Am. Chem. Soc.* **2011**, *133*, 5389.
(47) Yu, J. H.; Joo, J.; Park, H. M.; Baik, S.-I.; Kim, Y. W.; Kim, S. C.; Hyeon, T. Synthesis of Quantum-Sized Cubic ZnS Nanorods by the Oriented Attachment Mechanism. *J. Am. Chem. Soc.* **2005**, *127*, 5662.
(48) Duan, L. M.; Quan, Z. W.; Yang, P. P.; Wang, H.; Lin, J. Shape-Controlled Synthesis of Wurtzite ZnS Microstructures Under Mild Solvothermal Condition. *J. Nanosci. Nanotechnol.* **2009**, *9*, 919.
(49) Motlan; Zhu, G.; Drozdowicz-Tomsia, K.; McBean, K.; Phillips, M. R.; Goldys, E. M. Annealing of ZnS nanocrystals grown by colloidal synthesis. *Opt. Mater.* **2007**, *29*, 1579.
(50) Shin, S. W.; Agawane, G. L.; Gang, M. G.; Moholkar, A. V.; Moon, J.-H.; Kim, J. H.; Lee, J. Y. Preparation and characteristics of chemical bath deposited ZnS thin films: Effects of different complexing agents. *J. Alloys Compd.* **2012**, *526*, 25.
(51) Nascimento, C. C.; Andrade, G. R. S.; Neves, E. C.; Barbosa, C. D. A. E. S.; Costa, L. P.; Barreto, L. S.; Gimenez, I. F. Nanocomposites of CdS Nanocrystals with Montmorillonite Functionalized with Thiourea Derivatives and Their Use in Photocatalysis. *J. Phys. Chem. C* **2012**, *116*, 21992.
(52) Higgins, E. P. C.; McAdams, S. G.; Hopkinson, D. G.; Byrne, C.; Walton, A. S.; Lewis, D. J.; Dryfe, R. A. W. Room-Temperature Production of Nanocrystalline Molybdenum Disulfide (MoS_2) at the Liquid-Liquid Interface *Chem. Mater.* **2019**, *31*, 5384.
(53) Monteiro, O. C.; Nogueira, H. I. S.; Trindade, T.; Motevalli, M. Use of Dialkyldithiocarbamato Complexes of Bismuth(III) for the Preparation of Nano- and Microsized Bi_2S_3 Particles and the X-ray Crystal Structures of $[Bi\{S_2CN(CH_3)(C_6H_{13})\}_3]$ and $[Bi\{S_2CN(CH_3)(C_6H_{13})\}_3(C_{12}H_8N_2)]$. *Chem. Mater.* **2001**, *13*, 2103−2111.
(54) Zeng, N.; Hopkinson, D. G.; Spencer, B. F.; McAdams, S. G.; Tedstone, A. A.; Haigh, S. J.; Lewis, D. J. Direct synthesis of MoS_2 or MoO_3 via thermolysis of a dialkyl dithiocarbamato molybdenum(IV) complex. *Chem. Commun.* **2019**, *55*, 99.
(55) García-Rodríguez, R.; Hendricks, M. P.; Cossairt, B. M.; Liu, H.; Owen, J. S. Conversion Reactions of Cadmium Chalcogenide Nanocrystal Precursors. *Chem. Mater.* **2013**, *25*, 1233.
(56) Kahn, M. L.; Glaria, A.; Pages, C.; Monge, M.; Saint Macary, L.; Maisonnat, A.; Chaudret, B. Organometallic chemistry: an alternative approach towards metal oxide nanoparticles. *J. Mater. Chem.* **2009**, *19*, 4044.
(57) Champouret, Y.; Spataro, G.; Coppel, Y.; Gauffre, F.; Kahn, M. L. Nanocrystal-ligands interaction deciphered: the influence of HSAB and pK_a in the case of luminescent ZnO. *Nanoscale Adv.* **2020**, *2*, 1046−1053.
(58) Spataro, G.; Champouret, Y.; Coppel, Y.; Kahn, M. L. Prominence of the instability of a stabilizing agent in the changes in physical state of a hybrid nanomaterial. *Chem. Phys. Chem.* **2020**, *21*, 2454.
(59) Du, Y.; Yin, Z.; Zhu, J.; Huang, X.; Wu, X.-J.; Zeng, Z.; Yan, Q.; Zhang, H. A general method for the large-scale synthesis of uniform ultrathin metal sulphide nanocrystals. *Nature Commun.* **2012**, *3*, 1177.
(60) Zheng, Z.; Butynska, R.; Serrano, C. V.; Marty, J.-D.; Mingotaud, C.; Kahn, M. L. One-Step Synthesis of Hybrid Liquid-Crystal ZnO Nanoparticles: Existence of a Critical Temperature Associated with the Anisotropy of the Nanoparticles. *Chem. − Eur. J.* **2016**, *22*, 15614.
(61) Li, J.; Xu, Y.; Wu, D.; Sun, Y. Novel Lamellar Mesostructured Zinc Sulfide Nanofibers. *Chem. Lett.* **2004**, *33*, 718.
(62) If the thickness is lower than a certain limit in the order of 2 nm, electron microscopy fails to give unambiguous information on the particle structure.
(63) Wang, X.; Shi, J.; Feng, Z.; Li, M. L.; Li, C. Visible emission characteristics from different defects of ZnS nanocrystals. *Phys. Chem. Chem. Phys.* **2011**, *13*, 4715.
(64) Sooklal, K.; Cullum, B. S.; Angel, S. M.; Murphy, C. J. Photophysical Properties of ZnS Nanoclusters with Spatially Localized Mn^{2+}. *J. Phys. Chem. A* **1996**, *100*, 4551.
(65) D'Amico, P.; Calzolari, A.; Ruini, A.; Catellani, A. New energy with ZnS: novel applications for a standard transparent compound. *Sci. Rep.* **2017**, *7*, 16805.
(66) Lippens, P. E.; Lannoo, M. Calculation of the band gap for small CdS and ZnS crystallites. *Phys. Rev. B* **1989**, *39*, 10935.
(67) Vogel, W.; Borse, P. H.; Kundu, M.; Kulkarni, S. K. Structure and Stability of Monodisperse 1.4-nm ZnS Particles Stabilized by Mercaptoethanol. *Langmuir* **2000**, *16*, 2032.
(68) Becker, W. G.; Bard, A. J. Photoluminescence and photo-induced oxygen adsorption of colloidal zinc sulfide dispersions. *J. Phys. Chem.* **1983**, *87*, 4888.
(69) Osman, M. A.; Othman, A. A.; El-Said, W. A.; Abd-Elrahim, A. G.; Abu-sehly, A. A. Thermal annealing and UV irradiation effects on structure, morphology, photoluminescence and optical absorption spectra of EDTA-capped ZnS nanoparticles. *J. Phys. D: Appl. Phys.* **2016**, *49*, No. 055304.
(70) Li, P.; Deng, S.; Zhang, L.; Liu, G.; Yu, J. Native point defects in ZnS: First-principles studies based on LDA, LDA + U and an extrapolation scheme. *Chem. Phys. Lett.* **2012**, *531*, 75.
(71) Tsakonas, C.; Thomas, C. B. Role of sulfur vacancies on the electrical characteristics of sputtered films of ZnS. *J. Appl. Phys.* **1995**, *78*, 6098.
(72) Wang, Q.; Trébosc, J.; Li, Y.; Lafon, O.; Xin, S.; Xu, J.; Hu, B.; Feng, N.; Amoureux, J.-P.; Deng, F. Uniform signal enhancement in MAS NMR of half-integer quadrupolar nuclei using quadruple-frequency sweeps. *J. Magn. Reson.* **2018**, *293*, 92.
(73) Larsen, F. H.; Jakobsen, H. J.; Ellis, P. D.; Nielsen, N. C. Sensitivity-Enhanced Quadrupolar-Echo NMR of Half-Integer Quadrupolar Nuclei. Magnitudes and Relative Orientation of Chemical Shielding and Quadrupolar Coupling Tensors. *J. Phys. Chem. A* **1997**, *101*, 8597.
(74) d'Espinose de Lacaillerie, J.-B.; Fretigny, C.; Massiot, D. MAS NMR spectra of quadrupolar nuclei in disordered solids: The Czjzek model. *J. Magn. Reson.* **2008**, *192*, 244−251.
(75) Wu, G. Zinc-67 nuclear magnetic resonance spectroscopy of solids. *Chem. Phys. Lett.* **1998**, *298*, 375.
(76) Eckert, H.; Yesinowski, J. P. Sulfur-33 NMR at natural abundance in solids. *J. Am. Chem. Soc.* **1986**, *108*, 2140.
(77) Musio, R. Applications of ^{33}S NMR Spectroscopy. *Annu. Rep. NMR Spectrosc.* **2009**, *68*, 1.
(78) Wagler, T. A.; Daunch, W. A.; Rinaldi, P. L.; Palmer, A. R. Solid State ^{33}S NMR of Inorganic Sulfides. *J. Magn. Reson.* **2003**, *161*, 191.
(79) Nagashima, H.; Trébosc, J.; Kon, Y.; Lafon, O.; Amoureux, J.-P. Efficient transfer of DNP-enhanced ^1H magnetization to half-integer

quadrupolar nuclei in solids at moderate spinning rate. *Magn. Reson. Chem.* **2021**, *59*, 920.
(80) Hall, D. A.; Maus, D. C.; Gerfen, G. J.; Inati, S. J.; Becerra, L. R.; Dahlquist, F. W.; Griffin, R. G. Polarization-Enhanced NMR Spectroscopy of Biomolecules in Frozen Solution. *Science* **1997**, *276*, 930.
(81) Lesage, A.; Lelli, M.; Gajan, D.; Caporini, M. A.; Vitzthum, V.; Miéville, P.; Alauzun, J.; Roussey, A.; Thieuleux, C.; Mehdi, A.; et al. Surface Enhanced NMR Spectroscopy by Dynamic Nuclear Polarization. *J. Am. Chem. Soc.* **2010**, *132*, 15459.
(82) Hope, M. A.; Halat, D. M.; Magusin, P. C. M. M.; Paul, S.; Peng, L.; Grey, C. P. Surface-selective direct ^{17}O DNP NMR of CeO_2 nanoparticles. *Chem. Commun.* **2017**, *53*, 2142.

https://doi.org/10.1021/acs.jpcc.3c02754
J. Phys. Chem. C 2023, 127, 17809−17819